Title

Monocular 3D Probe Tracking for Generating Sub-Surface Optical Property Maps From Diffuse Optical Spectroscopic Imaging

Journal

IEEE Transactions on Biomedical Engineering, 67(7)

ISSN

0018-9294

Authors

Amelard, Robert
Lam, Jesse H
Hill, Brian
et al.

Publication Date

2020-07-01

DOI

10.1109/tbme.2019.2950004

Peer reviewed

Monocular 3D Probe Tracking for Generating Sub-Surface Optical Property Maps From Diffuse Optical Spectroscopic Imaging

Robert Amelard, Member, IEEE, Jesse H. Lam, Brian Hill, Amanda Durkin, Kyle Cutler, and Bruce J. Tromberg

Abstract—Objective: Diffuse optical spectroscopic imaging (DOSI) is a promising biophotonic technology for clinical tissue assessment, but is currently hampered by difficult wide area assessment. A co-integrative optical imaging system is proposed for dense sub-surface optical property spatial assessment. Methods: The proposed system fuses a co-aligned set of camera frames and diffuse optical spectroscopy measurements to generate spatial sub-surface optical property maps. A 3D rigid body motion estimation model was developed by fitting automatically detected target features to an *a priori* geometric model using a single overhead camera. Point-wise optical properties were measured across the tissue using frequency domain photon migration DOSI. The 3D probe trajectory and temporal optical property data were fused to generate 2D spatial optical property maps, which were projected onto the tissue image using pre-calibrated camera parameters. Results: The system demonstrated sub-millimeter positional accuracy (error 0.24 $\pm$ 0.35 mm) across different probe speeds (1.0–3.8 cm/s), and displacement accuracy in overhead (0.42 $\pm$ 0.33 mm) and tilted (0.51 $\pm$ 0.51 mm) camera orientations. Unstructured scans on a tumor inclusion phantom showed strong contrast under different probe paths, and significant ($p < 0.001$) changes in optical properties in an *in vivo* leg cuff occlusion protocol with spatial anatomy localization. Conclusion: The proposed co-integrative optical imaging system generated dense sub-surface optical property distributions across wide tissue areas with sub-millimeter accuracy at different probe speeds and trajectories, and does not require pre-planned probe route for tissue assessment. Significance: This system provides a valuable tool for real-time non-invasive tissue health and cancer screening, and enables longitudinal disease progression assessment through unstructured probe-based optical tissue assessment.

I. INTRODUCTION

ASSESSING tissue properties is important for maximizing diagnostic and therapeutic efficacy. Optical imaging systems assess tissue composition and structure across spatial scales using non-invasive light-based techniques. Diffuse optical spectroscopic imaging (DOSI) quantitatively measures sub-surface interactions of light with tissue for inferring optical properties, more specifically, scattering (μ_s') and absorption (μ_a) coefficients, which are then used to assess concentrations of bulk absorbing tissue chromophores, primarily oxyhemoglobin (HbO_2), deoxyhemoglobin (Hb), water (H_2O), and lipid [1]. In combination, these quantities reflect aspects of tissue perfusion, metabolism, hydration and blood volume [2], and provide clinically relevant information for assessing tissue health in applications such as breast cancer [3], bone sarcoma [4], and acute hemorrhage treatment [5].

Traditionally, DOSI operates as a point-measurement device, wherein a probe is affixed to a single location and tissue chromophores are tracked over time to assess functional tissue changes. Additional spatial coverage may provide increased clinical insight into localized tissue function, such as physiological responses to exercise [6], weight loss [2], and chemotherapy treatment in breast cancer research [7]. However, these methods generally suffer from low spatial resolution and laborious spatial sampling, usually by drawing a fixed landmark-based grid pattern on the tissue [8]–[10]. Additionally, longitudinal follow-up may be error-prone due to landmark-based registration. Other methods have incorporated an array of source-detector pairings for simultaneous spatial coverage for breast cancer [11] and critical care [12] monitoring, but these systems have fixed spatial resolution and form factor, making generalized free-form imaging challenging.

To detach from the fixed grid approach and enable free-form unstructured scanning across an area of interest, spatial context must be detected and co-processed with temporal DOSI measurements. Spatial object tracking has been studied in other fields, primarily using either inertial measurement units (IMUs) or video-based object tracking. IMUs use a combination of accelerometers, gyroscopes, and magnetometers to compute the body's relative orientation in space. These devices have been used to track 3D movement in applications such as lower limb biomechanical analysis [13] and robotic microsurgery tremor compensation [14]. However, IMUs provide relative changes in orientation, and require further instrumentation for estimating a probe measurement in the global spatial context of a tissue region of interest. Image-based object tracking algorithms are able to track objects in space with visual global context. Recent developments in deep learning have enabled robust single-camera object tracking algorithms [15], [16], however inferring 3D position with high accuracy is challenging. Multi-camera approaches can yield high 3D accuracy for challenging scenarios such as stereoscopic tracking of intra-operative tools [17] and marker-based motion joint tracking [18], but these approaches are generally bulky and expensive, making them infeasible in clinical settings.

To address these outstanding challenges, we propose a co-integrative single camera-based DOSI imaging system. This system enables generation of sub-surface optical property maps by tracking the 3D probe trajectory across tissue using a single camera and an embedded physical *a priori* target pattern with known geometric features. By incorporating the *a priori* target pattern model into a computational rigid body tracking framework, the 3D probe trajectory can be estimated and fused with the temporal optical property measurements to generate a 2D optical property map across the scanned area. The proposed computational framework can be used with any camera through a one-time calibration procedure, and does not require a pre-planned (e.g., grid) probe route.

The remainder of the paper is organized as follows. Section II presents relevant diffuse optical spectroscopic imaging theory and the computational framework for 3D probe measurement tracking. Section III presents experimental results using an optical tissue tumor inclusion phantom and in vivo leg occlusion protocol. Section IV presents discussion on the *in vivo* dense optical property maps and tracking coordinate systems. Section V concludes the work.

II. METHODS

Given a co-aligned set of frames *I(x, y, t)* and point-based temporal measurements *o*(*t*), where *o*(*t*) is an optical property of interest (e.g., absorption, scattering, chromophore concentration), the goal was to generate a dense 2D sub-surface optical property map *O*(*x, y*) using estimates of the 3D probe measurement location coordinates (x_m (*t*), y_m (*t*), z_m (*t*)) at each time point *t*. The problem was posed as a rigid body probe planar motion estimation problem. Using a single overhead camera, the probe was tracked by detecting a planar checkerboard pattern printed on the top probe face. Tissue optical properties were assessed at non-gridded positions across the tissue using a frequency domain photon migration diffuse optical spectroscopic imaging (DOSI) system. Fig. 1 shows a graphical overview of the system components.

A. Diffuse Optical Spectroscopic Imaging (DOSI)

DOSI uses frequency domain photon migration (FDPM) with computational models to assess absolute optical properties from turbid media [1]. Sinusoidal temporally modulated near-infrared (NIR) laser light was illuminated into turbid media. The recovered optical signal, through the use of an avalanche photodiode (APD), was compared to a reference, and the amplitude decay A(ω, ρ) and phase delay $\Theta(\omega, \rho)$ was calculated across a broad bandwidth frequency sweep ($\omega \in [50, 500]$ MHz) at a source-detector separation ρ. Calibration was achieved by use of silicone-based tissue simulating phantoms [19]. The calibrated amplitude and phase for each wavelength was then fit using a P1 semi-infinite approximation to the radiative transport equation yielding absolute optical absorption (μ_a) and reduced scattering (μ'_s) coefficients [20]. Tissue chromophore concentrations Ci were then extracted from μ_a given tabulated extinction coefficients for each absorbing species E_i by use of linear least-squares fitting against a Beer-Lambert formulation:

$$\mu_a(\lambda) = 2.303 \sum_i \epsilon_i(\lambda) C_i$$

Similarly, the scattering spectra $\mu'_s(\lambda)$ was estimated by a least-squares fit to a power law inspired by Mie theory:

$$\mu'_s(\lambda) = a\lambda^{-b}$$

Then, multiple optical properties were monitored for generating a dense sub-surface optical property map:

$$o(t) \in \{\mu a\ (t),\ \mu'_s\ (t), HbO_2\ (t), Hb(t), THC(t),\ SO_2\ (t)\} \qquad (3)$$

where HbO_2 (t), Hb(t), THC(t), SO_2 (t) are oxyhemoglobin concentration, deoxyhemoglobin concentration, total hemoglobin concentration, and blood oxygen saturation percentage, respectively, yielded from NIR spectroscopic decomposition.

FDPM measurements were accomplished by routing laser light (727 nm, 787 nm, 832 nm) to the sample using an optical fiber bundle comprised of eight 0.37 NA, 400 μm optical fibers. The laser intensity was set to 30 mW for all wavelengths controlled by a laser diode controller (LDC-3916, Newport, Irvine, CA). Modulation frequencies ranged from 50–400 MHz, and amplitude and phase sampling was provided by a network analyzer (TR1300/1, Copper Mountain Inc. Indianapolis, IN). Laser light was collected using an APD (S11519-30 APD with custom module, Hamamatsu Photonics, Hamamatsu Japan).

B. 3D Measurement Coordinate Estimation

This section adopts the notation ${}^{s}\vec{p}$ to declare the coordinate system s for a specified coordinate point $\vec{p}$ (e.g., w p_ is a point ${}^{w}\vec{p}$ in the world coordinate system). Likewise, transformation matrices from coordinate system a to b are written as ${}^{b}_{a}M$. The three coordinate systems used throughout are the world coordinate system W, defined by the probe position; camera coordinate system C, a fixed coordinate system defined by the position and orientation of the camera; and image coordinate system I, a 2D coordinate system on the imaging plane. See Fig. 1 for a graphical depiction.

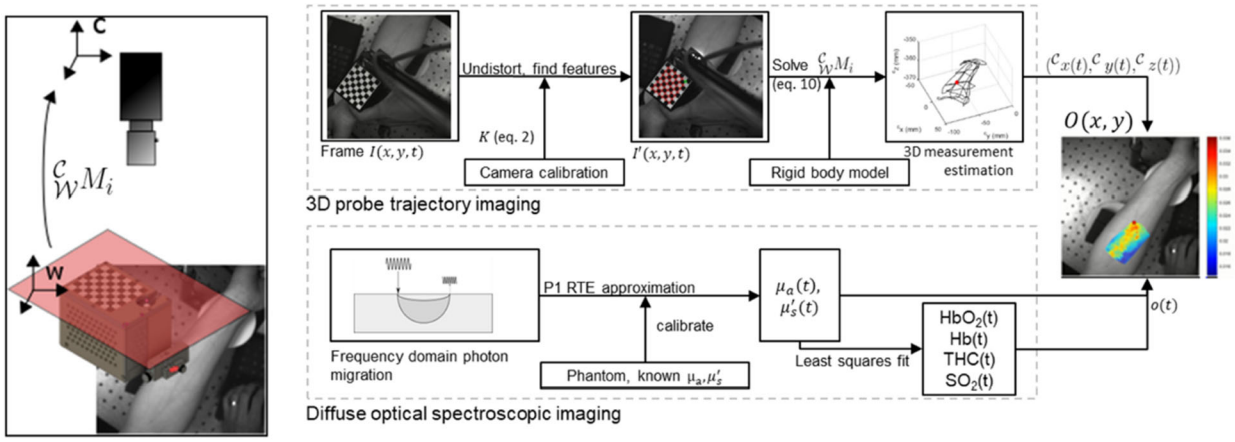

Fig. 1. System diagram showing the primary processing steps. An overhead single-camera tracking system and diffuse optical spectroscopic imaging (DOSI) were fused into a co-integrative optical system for non-gridded dense wide area optical property map generation. DOSI (bottom panel) employs a frequency domain photon migration model with calibrated phantom measurements for assessing optical properties at a single location. An overhead camera was used to collect frames of the probe trajectory (top panel). By embedding an *a priori* target model on the probe, the rigid body motion of the probe was estimated by solving a least-squares optimization of the measured, undistorted target features and a theoretical rigid body model, yielding the 3D probe measurement coordinate in the fixed camera coordinate system. These information were fused to generate a spatiotemporal optical property map.

1) Problem Formulation: The probe tracking problem was posed as a 3D rigid body transformation estimation problem. That is, for each frame *I(x, y, t)* at time t, the probe's orientation in the 3D world coordinate system was estimated according to a 3D rigid transformation of the probe in the scene (i.e., rotation and translation).

Mathematically, given a set of 2D feature points in the calibrated image plane ${}^{\mathcal{I}}P = \{{}^{\mathcal{I}}\vec{p}_i\}$, a transformation function Ω was sought that optimally transforms the apriori3D target model feature points in world coordinates ${}^{\mathcal{W}}P = \{{}^{\mathcal{W}}\vec{p}_i\}_i$ into the a posteriori 2D detected feature points ${}^{\mathcal{I}}P$ in a least-squares manner:

$$\arg\min_{\Omega} \sum_i \left\| {}^{\mathcal{I}}\vec{p}_i - \Omega\left({}^{\mathcal{W}}\vec{p}_i\right) \right\|_2$$

To impose the physical constraints of a 3D rigid body traveling in the scene, the transformation function Ω was modeled as a rigid body transformation matrix ${}^{\mathcal{I}}_{\mathcal{W}}M$:

$$\arg\min_{{}^{\mathcal{I}}_{\mathcal{W}}M} \sum_i \left\| {}^{\mathcal{I}}\vec{p}_i - {}^{\mathcal{I}}_{\mathcal{W}}M \ {}^{\mathcal{W}}\vec{p}_i \right\|_2$$

The goal, therefore, was to determine ${}^{\mathcal{I}}_{\mathcal{W}}M$ by detecting target model feature points in the image and incorporating *a priori* target model knowledge into an estimation model.

2) Camera Calibration and Probe Tracking: To ensure homogeneously spaced pixel distances, the imaging system's optical distortion was removed through a two-coefficient radial distortion model using a two-step optimization approach [21]. Specifically, the camera was modeled as a pinhole camera with initially) zero lens distortion:

$$\alpha \begin{bmatrix} {}^{\mathcal{I}}x \\ {}^{\mathcal{I}}y \\ 1 \end{bmatrix} = K \ {}^{\mathcal{C}}_{\mathcal{W}}M \begin{bmatrix} {}^{\mathcal{W}}x \\ {}^{\mathcal{W}}y \\ {}^{\mathcal{W}}z \\ 1 \end{bmatrix} \qquad (6)$$

where α is an arbitrary scale factor, ${}^{\mathcal{C}}_{\mathcal{W}}M$ is the extrinsic camera matrix, and *K* is the intrinsic camera matrix with five degrees of freedom:

$$K = \begin{bmatrix} f_x & s & {}^{\mathcal{I}}x_0 \\ 0 & f_y & {}^{\mathcal{I}}y_0 \\ 0 & 0 & 1 \end{bmatrix} \qquad (7)$$

where (f_x ,f_y) is the focal length, s is skew, and ($^I x_0$,$^I y_0$) is the principle point in the image plane. Camera parameters were determined by initially solving a closed-form solution assuming zero lens distortion, and then refining this solution with a two-coefficient radial distortion model through nonlinear least squares minimization [21], [22]. The intrinsic camera matrix and distortion variables were stored and used to process all the subsequent frames.

Using the solved radial distortion variables to invert the effects of lens distortion across all frames [21], the goal was to estimate the 3D position of the probe measurement location by tracking the 2D feature model points. An 8 × 7 checker-board target model with 6.5 mm spacing was used as the target model, and placed on the top probe face to provide salient tar-get model features with known planar spatial characteristics for high-contrast tracking. Checkerboard corner positions $^C p_{ij}$ were automatically detected in the camera coordinate system on the rectified frames $I'(x, y, t)$ using multi-orientation corner kernel convolution with sub-pixel localization [23]. Specifically, four corner filter kernels $\{A, B, C, D\}$ were constructed to detect center-pixel corners. These kernels were rotated to provide robustness to different orientations. By convolving the image with the filters, the filter response f^{θ}_X of kernel X ∈ $\{A, B, C, D\}$ and orientation θ were used to generate a corner likelihood map:

$$C = \max\left(\max_{\theta}\left(S_1^{\theta}\right), \max_{\theta}\left(S_2^{\theta}\right)\right) \qquad (8)$$

where S_1^{θ} and S_2^{θ} denote the corner likelihood at a pixel under the two possible flippings. The final set of corner coordinates P_C were determined through non-maxima suppression thresholding and iterative seed point expansion [23]. Due to the recti-fication process, these corner positions result from a projection transformation of an equally spaced planar grid that has been rotated and translated in the world coordinate system. A total of 42 feature points allowed for sufficient redundancy to robustly estimate the plane model. By embedding an *a priori* geometric target model in the scene, a single camera solution is proposed to estimate 3D feature coordinates by computing the effect of 3D transformation of the model feature points.

3) Compute 3D World Transformation: Given the fixed intrinsic camera matrix K, the goal was to compute the trans-formation matrix ${}^{C}_{W}M_i$ of the probe for frame $I'(x, y, t_i)$ to estimate the 3D measurement location in the fixed 3D camera co-ordinate system. Specifically,

$$\begin{bmatrix} {}^{C}x \\ {}^{C}y \\ {}^{C}z \\ 1 \end{bmatrix} = {}^{C}_{W}M_i \begin{bmatrix} {}^{W}x \\ {}^{W}y \\ {}^{W}z \\ 1 \end{bmatrix} \qquad (9)$$

The transformation matrix ${}^{C}_{W}M_i$ is described by the translation of the optical center from world coordinates to 3D camera coordinates, and rotation of the image plane:

$$ {}^{C}_{W}M_i = \begin{bmatrix} r_0 & r_1 & r_2 & t_x \\ r_3 & r_4 & r_5 & t_y \\ r_6 & r_7 & r_8 & t_z \\ 0 & 0 & 0 & 1 \end{bmatrix} \tag{10} $$

Given a calibrated camera, the relationship between the *j*th pattern feature coordinate in the world space ${}^{W}\vec{p}_{ij}$ and the detected feature points in the image space ${}^{I}\vec{p}_{ij} \in$ PC was modeled by a projective transformation:

$$ \gamma \begin{bmatrix} {}^{W}x_{ij} \\ {}^{W}y_{ij} \\ 0 \\ 1 \end{bmatrix} = H_i \begin{bmatrix} {}^{I}x_{ij} \\ {}^{I}y_{ij} \\ 1 \end{bmatrix} \tag{11} $$

where γ is an arbitrary scaling parameter, and H_i is the projective transformation homography matrix:

$$ H = \begin{bmatrix} h_{11} & h_{12} & h_{13} \\ h_{21} & h_{22} & h_{23} \\ h_{31} & h_{32} & 1 \end{bmatrix} \tag{12} $$

Note the 0 entry in the world coordinates in Eq. (11), since the ^{W}z axis was defined as orthogonal to the target plane, and thus all feature points lie on the z =0 plane. The extrinsic rotation and translation matrices were computed using a closed form planar estimation solution [21]:

$$ \lambda = \frac{1}{||K^{-1} \begin{bmatrix} h_{11} & h_{21} & h_{31} \end{bmatrix}^T ||}, \tag{13} $$

$$ {}^{C}_{W}R = \begin{bmatrix} | & | & | \\ \lambda K^{-1}h_1 & \lambda K^{-1}h_2 & \lambda K^{-1}h_1 \times \lambda K^{-1}h_2 \\ | & | & | \end{bmatrix}, \tag{14} $$

$$ {}^{C}_{W}T = \lambda K^{-1} \begin{bmatrix} h_{13} \\ h_{23} \\ h_{33} \end{bmatrix} \tag{15} $$

where h_k is the k^{th} column vector of matrix H_i from Eq. (12). This closed-form estimate may still be sensitive to estimation noise. Local iterative optimization was performed using the closed-form solution as the original solution estimation, making it reliable and fast convergence. Specifically, the rigid body motion parameters were solved simultaneously using Levenberg-

Marquardt iterative non-linear least-squares minimization, using the following objective function:

$$ {}^{C}_{W}\hat{M}_i = \arg\min_{{}^{C}_{W}M_i} \sum_j \left\| {}^{I}\vec{p}_{ij} - \underbrace{{}^{I}_{C}(KQ){}^{C}_{W}M_i}_{{}^{I}_{W}M} \; {}^{W}\vec{p}_{ij} \right\|_2 \qquad (16) $$

where K is the intrinsic camera matrix from Eq. (7), Q is the projection matrix $\mathbb{1}_{3\times4}$, ${}^{C}_{W}M$ is the rigid body trans-formation matrix from Eq. (10), and ${}^{I}\vec{p}_{ij} = [{}^{I}x_{ij} \;\; {}^{I}y_{ij} \;\; \bar{1}]^T$ ${}^{W}\vec{p}_{ij} = [{}^{W}x_{ij} \;\; {}^{W}y_{ij} \;\; {}^{W}z_{ij} \;\; \bar{1}]^T$ are points in the 2D image plane and 3D world coordinate systems, respectively, in homogeneous coordinates. The term ${}^{I}_{W}M$ shows the final formulation of the feature point transformation matrix, which is used to solve Eq. (5).

The final probe measurement coordinate was determined halfway between the source and detector. This location was computed as a 3D offset ${}^{w}\Delta_s = (\delta_x, \delta_y, \delta_z)$ from the world co-ordinate origin using measurements from the 3D probe design model, yielding ${}^{W}\vec{p}_s = {}^{W}\vec{p}_o + {}^{W}\Delta_s$, where ${}^{W}\vec{p}_o$ is the origin of the world coordinate system. The probe measurement location ${}^{C}\vec{p}_s(t_i)$ in the camera coordinate system was computed for each time t_i by applying the solved rigid body transformation matrix from Eq. (16):

$$ {}^{C}\vec{p}_s(t_i) = {}^{C}_{W}M_i \;\; {}^{W}\vec{p}_s(t_i) \qquad (17) $$

C. Spatiotemporal Optical Property Sampling

The sequence of 3D probe measurement coordinates $\{({}^{C}x_i, {}^{C}y_i, {}^{C}z_i) \mid i=[0,n]\}$, or conversely the projected 2D im-age plane coordinates $\{({}^{I}x_i, {}^{I}y_i) \mid i=[0,n]\}$, and DOSI optical property measurements $\{oj \mid j=[0,m]\}$ (from Eq. (3)) may be captured at different sampling rates. Furthermore, while the camera frame rate is constant, DOSI measurements may be collected at non-uniform sampling times. Assuming that DOSI measurements are collected progressively across a tissue, and thus assuming piecewise continuous measurements, the DOSI measurements were interpolated using a cubic spline interpolation to yield an interpolated $\{o'_i \mid i=[0,n]\}$ discrete signal with equal sampling frequency as the camera coordinate measurements. The optical property map $O(x, y)$ was then computed using triangle-based bicubic interpolation of the non-gridded scattered measurements [24], [25]. Thus, for each pixel coordinate (x_i, y_i) in the final map $O(x, y)$, the interpolated tissue optical property measurements were collected from its neighborhood Ni as determined by Delaunay triangulation.

D. Experimental Setup

Positional accuracy was evaluated against a pre-programmed path using a motorized XY stage over a tissue phantom. The XY stage moved the probe across the phantom in 8 cm sweeps and 1 cm steps, covering a total path distance of 80 cm over a 64 cm^2 area. The effect of both probe speed and probe translation was evaluated. Error of the estimated 3D probe coordinate was computed through the Euclidean distance of the estimated and true location for each frame by sampling the known (pre-programmed) path. Accuracy was calculated by computing the correlation, agreement and absolute error between the known pre-programmed path and the estimated 3D probe trajectory.

Sub-surface optical property maps were generated for both a breast tumor inclusion optical phantom model, as well as an *in vivo* thigh cuff inflation protocol. These different tissue characteristics were used to demonstrate the ability to scan and detect clinically relevant scanning output. The heterogenous silicone-based tissue phantom was fabricated to simulate the absorption-scattering contrast ratio typical of a breast tumor [26]. It contained a 26 mm diameter absorbing hemispherical inclusion embedded 9 mm below the phantom surface, measured at the top of the inclusion. The phantom was formulated using a silicone rubber base (P4, Eager Polymers, Chicago, IL) with water-soluble Nigrosin dye (Sigma-Aldrich, St. Louis, MO) as the primary absorber and anatase titanium (IV) dioxide (Sigma-Aldrich, St. Louis, MO) as the primary scattering agent. The construction process followed similar instructions reported previously [19]. However, prior to the silicone curing step, a hemi-spherical, highly absorbing inclusion was suspended below the surface of the larger phantom in order to simulate an embedded tumor. The absorption and scattering coefficients were characterized at 785 nm using the compound concentrations for the inclusion (μa = 0.02 mm^{-1} , $\mu's$ = 0.7 mm^{-1}) and background (μa = 0.006 mm^{-1} , $\mu's$ = 0.7 mm^{-1}).

A thigh cuff occlusion protocol was performed to evaluate changes in perfusion in a vascular occlusion model. The participant assumed a face-down supine position on a bed. The camera was placed over the lower legs, facing directly down. DOSI scans were performed on both legs, covering the gastrocnemius and soleus muscle groups. Two trials were performed. First, a normal baseline scan was performed on both legs to determine baseline optical properties. Second, a thigh cuff was placed around the left thigh, and inflated beyond systolic blood pressure to restrict both arterial and venous flow. DOSI scans were performed after 3 min of occlusion.

III. EXPERIMENTAL RESULTS

Fig. 2 shows an image of the experimental setup. A monochromatic camera (FLIR GS3-U3-41C6NIR) was mounted in a fixed position above the measurement area such that the field of view was sufficient to capture the entire path of the probe. Frames were acquired at 30 fps, with an exposure time of 4 ms. DOSI and the camera were time synchronized at the start of data acquisition. The system was evaluated for positional accuracy, and *in vivo* wide area optical property assessment during a cuff occlusion protocol. The human measurements were performed

under a clinical protocol approved by the Institutional Review Board at the University of California Irvine, and were performed in accordance with the Declaration of Helsinki.

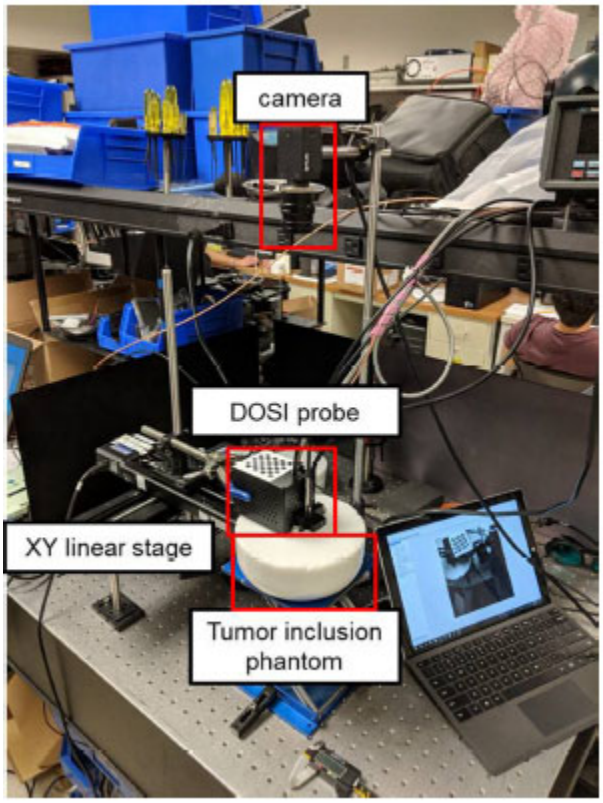

Fig. 2. Experimental setup. The camera was positioned overhead, facing down toward the DOSI probe. Here, the XY motorized stage is shown (see Section III-A).

A. Positional Accuracy

Fig. 3 shows the 3D probe position estimation evaluated at two different camera angles to show robustness to relative probe-camera positioning: overhead (Fig. 3(a–c)) and 20◦ tilt (Fig. 3(d –f)).

The estimated path displacement demonstrated high correlation and sub-millimeter accuracy across the whole path in both overhead ($r^2 = 0.9999$, error -0.42 ± 0.33 mm) and tilted ($r^2 = 0.9998$, error 0.51 ± 0.51 mm) camera orientations. Using the camera calibration matrix, the 3D path was projected onto the 2D image field of view (Fig. 3(c ,f)). Both paths showed the same spatiotemporal route across the tissue phantom, demonstrating robustness to relative camera-probe positioning for optical property visualization.

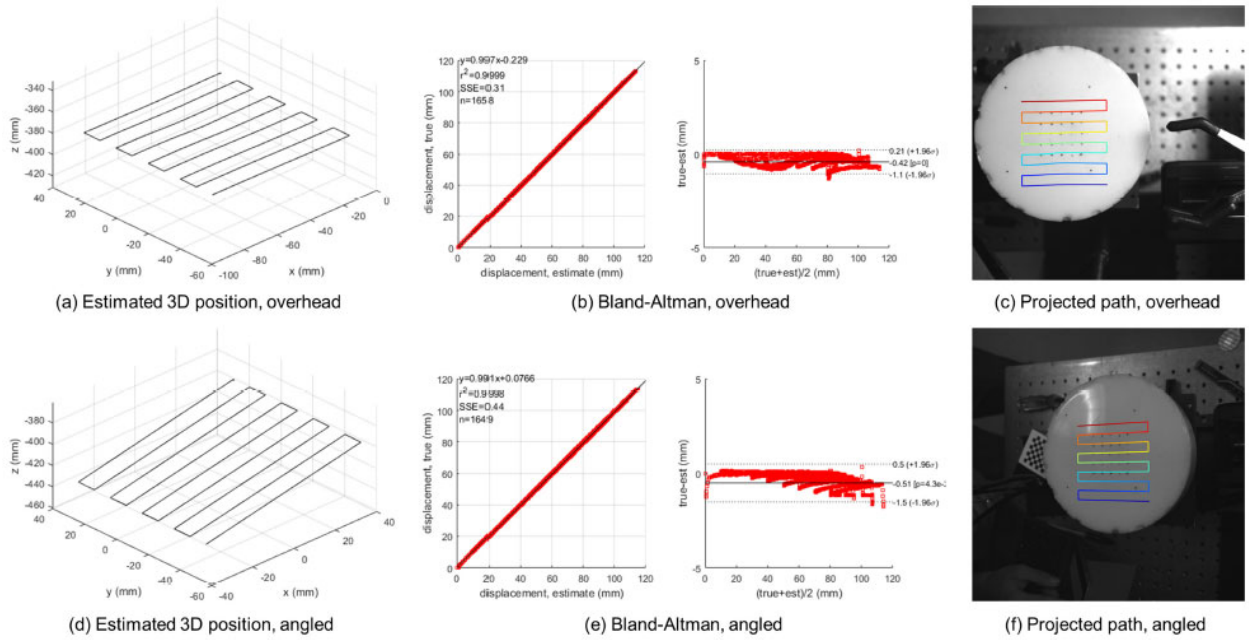

Fig. 3. 3D probe position estimation over a pre-programmed path, with the camera angled directly above (a–c) and at a 20◦ angle (d–f) relative to the tissue phantom. The estimated coordinates exhibited high agreement with the true programmed path for both overhead (r^2 = 0.9999, error -0.42 ± 0.33 mm) and angled (r^2 = 0.9998, error 0.51 ± 0.51 mm) camera orientations. The projected path (c, f) color coding denotes time (blue: start, red: finish).

The effect of probe movement speed on positional accuracy was evaluated at six different speeds, varying from 1.0 to 3.8 cm/s. Fig. 4 shows the distribution of 3D probe estimation errors across different probe operating speeds, and descriptive statistics are presented in Table I. The results show robustness of the position estimation system to different operating speeds, observed through a small range in error mean (0.33–0.37 mm), median (0.30–0.39 mm), interquartile range (0.44–0.52 mm), and pooled mean error (0.24 ± 0.35 mm) across all speeds.

The results demonstrated robustness to different operator scanning speeds, with sub-millimeter maximum errors (≤0.75 mm) across all speeds.

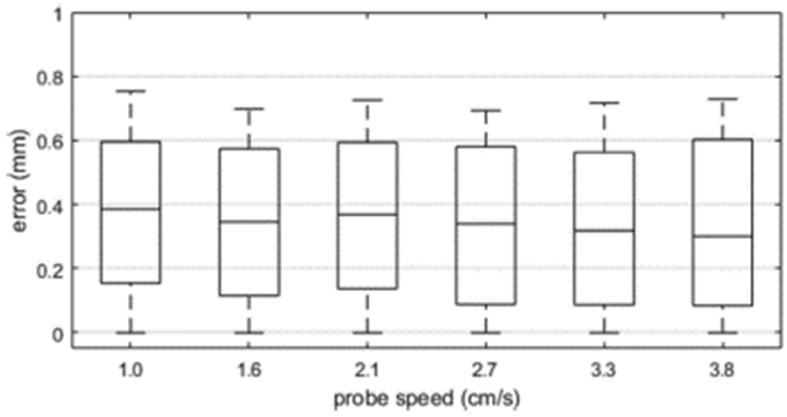

Fig. 4. 3D probe position estimation error distributions across different probe handling speeds. Probe sensor position accuracy was robust to speed increases from 1.0 to 3.8 cm/s, exhibiting max error < 0.8 mm for all speeds, and median error ranging from 0.39 mm (1.0 cm/s) to 0.30 mm (3.8 cm/s). See Table I for descriptive statistics.

TABLE I

STATISTICS OF 3D PROBE POSITION ESTIMATION ERROR ACROSS DIFFERENT PROBE HANDLING SPEEDS. (Q1–FIRST QUARTILE, Q3–THIRD QUARTILE, IQR–INTERQUARTILE RANGE)

	error (mm)						
probe speed	**mean**	**std**	**median**	**Q1**	**Q3**	**IQR**	**max**
1.0 cm/s	0.37	0.24	0.39	0.15	0.60	0.44	0.75
1.6 cm/s	0.34	0.23	0.35	0.12	0.57	0.46	0.70
2.1 cm/s	0.36	0.24	0.37	0.14	0.59	0.46	0.73
2.7 cm/s	0.33	0.24	0.34	0.09	0.58	0.49	0.69
3.3 cm/s	0.33	0.25	0.32	0.09	0.56	0.48	0.72
3.8 cm/s	0.34	0.25	0.30	0.08	0.60	0.52	0.73

B. Optical Property Assessment

1) Breast Tumor Inclusion Model: Fig. 5 shows the result of freeform hand-operated DOSI scans using a tumor inclusion phantom (see Video 1 for the full capture). The scan was first performed at a coarse resolution (top row) to demonstrate rapid wide area tissue assessment. The coarse scan shows a sub-surface absorbing tumor inclusion with high absorbing and low scattering properties compared to the surrounding tissue. A fine resolution scanning path that emphasized the area of the highly absorbing medium was performed (bottom row) to demonstrate fine resolution investigation of heterogeneity. This fine resolution scan shows more structure of the absorbing tumor inclusion, and a finer resolution optical property map in the target area. These scans were performed without trajectory guidance, which can be seen in the coarse wide area probe trajectory (a) and circular trajectory (d).

2) Thigh Cuff Occlusion Protocol: Fig. 6 shows both left and right lower leg sub-surface optical property maps during normal control (top row) and occlusion (bottom row) manipulations (see Video 2 for the full capture). Absorption and scattering coefficients (μ_a , μ'_s) were extracted from the DOSI measurements, and absorption was further decomposed into concentrations of oxyhemoglobin, deoxyhemoglobin, total hemoglobin, and tissue oxygen saturation. The elimination of arterial supply and venous return in the left leg, combined with maintained muscle metabolic activity and capillary flow, resulted in changes in tissue perfusion and hemoglobin concentrations. Optical property values were assessed for statistical differences in normal vs occlusion states using a two-tailed paired-sample t-test (see Fig. 7). The effect of left leg occlusion resulted in statistically significant ($p< 0.001$) increases in scattering ($\Delta\overline{\mu'_s}$ = 0.06 mm^{-1}), absorption ($\Delta\overline{\mu_a}$ = 0.004 mm^{-1}), deoxyhemoglobin ($\Delta\overline{Hb}$ = 34.4 μM), and total hemoglobin ($\Delta\overline{THC}$ = 26.8 μM), as well as statistically significant ($p< 0.001$) decreases in oxyhemoglobin ($\Delta\overline{HbO_2}$ = −7.5 μM) and oxygen saturation ($\Delta\overline{SO_2}$ = −26.8%) in the left leg. This is commensurate with the effects of venous blood pooling and maintained metabolic activity resulting in the consumption of oxygen in muscles and tissues. There was also an effect of left leg occlusion on the right leg, with statistically significant increases in scattering ($\Delta\overline{\mu'_s}$ = 0.044 mm^{-1}), deoxyhemoglobin ($\Delta\overline{HbO}$ = 12.5 μM), and statistically significant ($p<0.001$) decreases in absorption ($\Delta\overline{\mu_a}$ = −0.002 mm^{-1}), oxyhemoglobin ($\Delta\overline{HbO_2}$ = −14.0 μM), and oxygen saturation ($\Delta\overline{SO_2}$ = −15.9%).

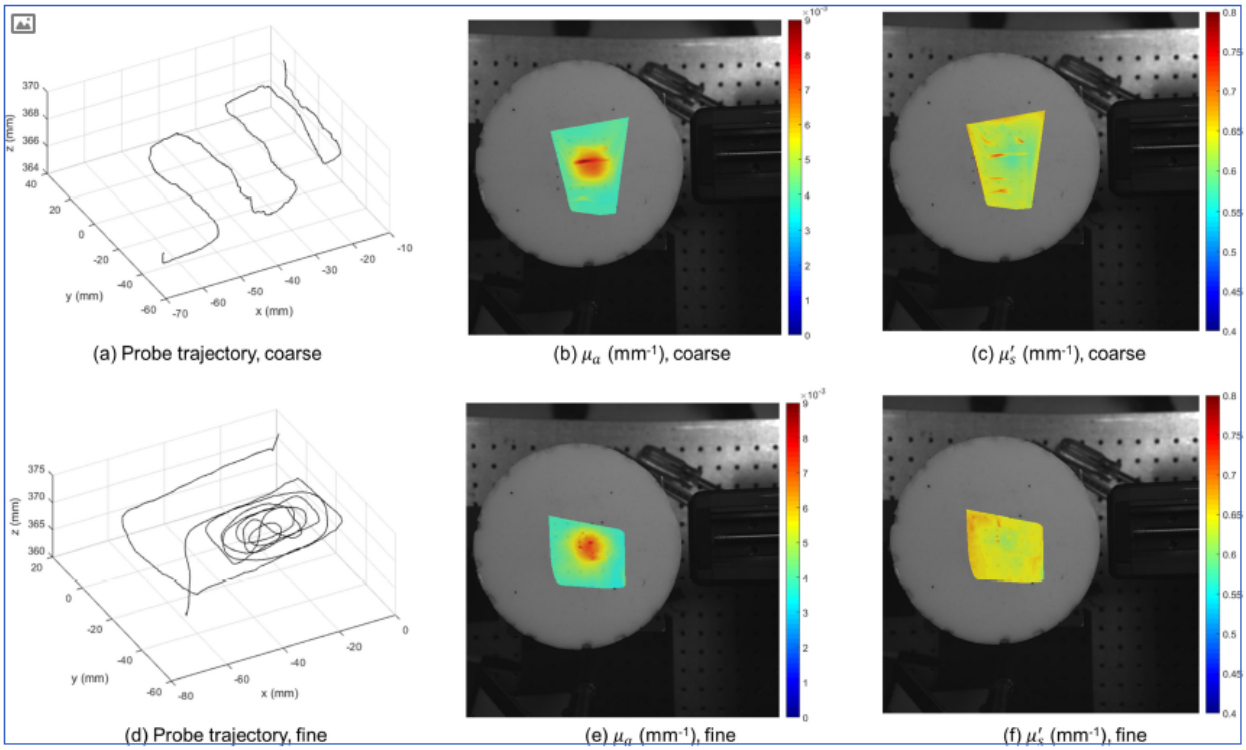

Fig. 5. Absorption (μ_a , 832 nm; b,e) and scattering ($\mu's$, 832 nm; c, f) maps of a tumor inclusion optical phantom constructed during freeform hand probe scanning (a, d). The phantom was scanned coarsely (a–c), and finely over a tumor inclusion (d–f). Coarse scanning allows for rapid tissue assessment, while fine scanning allows more high-resolution optical property assessment.

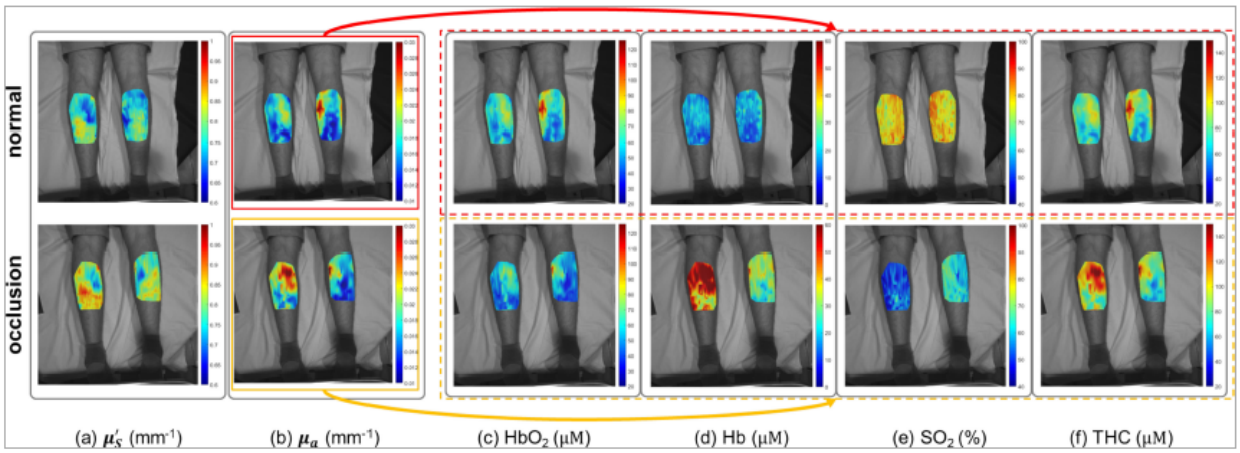

Fig. 6. Dense optical property maps from non-gridded freeform FDPM DOSI probe scanning of a thigh cuff occlusion protocol. A wide area of the left and right lower leg were scanned to assess perfusion changes in the calf when comparing left leg thigh cuff arterial occlusion (bottom row) to a normal control baseline (top row). Only the left leg was occluded. Left leg occlusion resulted in increased scattering (μ□s , 832 nm) (a) and absorption (μ_a , 832 nm) (b) compared to normal left leg. The gastrocnemius medial head was observed in both legs as a localized area of higher absorption and lower scattering. Absorption (μ_a) was further decomposed into concentrations of oxyhemoglobin (c), deoxyhemoglobin (d), tissue saturation (e), and total hemoglobin concentration (f). Left leg thigh cuff occlusion restricted venous return, and with sustained metabolic activity, resulted in increased deoxyhemoglobin concentration (d), reduced tissue oxygenation (e), and increased total hemoglobin due to vascular pooling (f). Statistical comparisons of the effects of control vs occlusion are presented in Fig. 7.

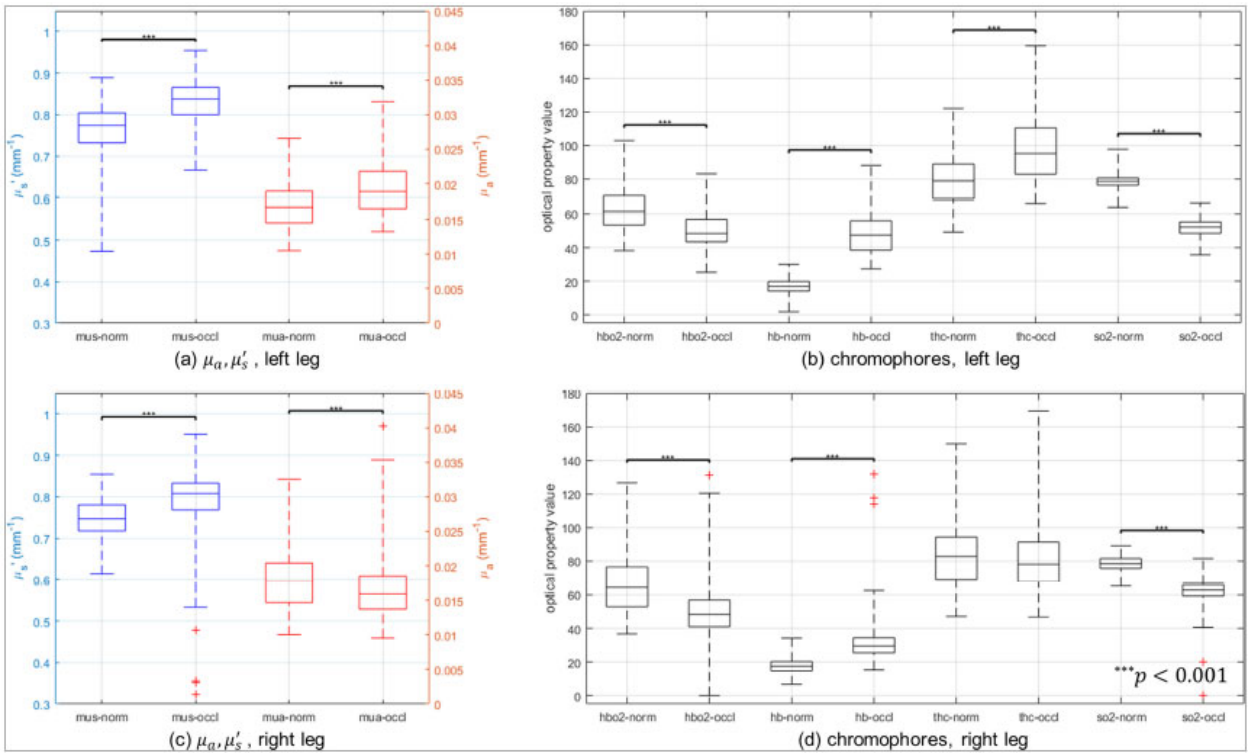

Fig. 7. Statistical comparisons of the changes in optical properties in left leg (top row) and right leg (bottom row) during normal control vs left leg occlusion. Left leg occlusion resulted in significant increases in scattering, absorption, deoxyhemoglobin, and total hemoglobin concentration, as well as significant decreases in oxyhemoglobin and oxygen saturation in the left leg. An effect was also observed in the right leg, with significant increases in scattering, deoxyhemoglobin, and decreases in absorption, oxyhemoglobin, and oxygen saturation. Associated spatial perfusion characteristics can be seen in Fig. 6.(***p< 0.001)

Additionally, heterogeneous spatial perfusion patterns were observed. The increase in μ_a upon occlusion was primarily observed at the location of gastrocnemius medial head, a large muscle group with high metabolic demand. A large increase in the muscle's localized deoxyhemoglobin concentration was observed as a result of maintained metabolic demand under restricted blood flow, as well as localized increase in total hemoglobin concentration resulting from localized blood pooling. In contrast, the oxygen saturation was reduced across the entire lower leg area, indicating whole region hypoperfusion. Apparent systemic changes were also observed in the right leg, with whole-area increases in deoxyhemoglobin and decreases in oxyhemoglobin compared to control. The total hemoglobin concentration remained relatively unchanged, indicating maintained blood flow through the right leg during left leg occlusion.

IV. DISCUSSION

The ability to generate sub-surface optical property maps from handheld freeform optical probe scanning has major implications in clinical disease screening and treatment effect monitoring. Although handheld biophotonic technologies have been shown to provide clinically relevant quantitative tissue proper-ties in a non-intrusive, safe (light-based) and handheld manner for applications such as breast cancer [3], bone sarcoma [4], and acute hemorrhage treatment [5], the clinical uptake of the technologies is currently limited by the lack of operator freedom, operator-patient interaction, and difficulty of landmark-based measurements for follow-up assessment. The demonstrated robustness to different probe operating speeds shows promise for the use of the technology by different operators, which is a critical characteristic for clinical adoption. Results presented here show the ability to rapidly assess tissue heterogeneity in a tissue tumor phantom, as well as assessing changes in vascular health and perfusion *in vivo* without needing to adhere to strict fixed probe routes. This new technology may enable effective assessment with the benefits of other widely adopted technologies, such as ultrasound imaging.

System accuracy is dependent on image resolution and the number of feature points in the target model. The mathematical formulation presented here generalizes to any asymmetric geometric model with known feature point distribution. Asymmetry is important to infer absolute orientation of the probe. De-creased resolution results in decreased feature point localization precision, and thus the optical setup (working distance, sensor size, focal length, etc.) is an important consideration. Theoretically, three feature points is sufficient to determine the planar orientation of the probe through the geometric fitting method. However, feature point redundancy provides increased accuracy to account for measurement and process inaccuracies at the expense of computation time. Here, an 8 × 7 checkerboard model empirically provided a desired accuracy-computation trade-off. The fitting procedure was modeled directly and used a physical motion model to explicitly determine the optimal orientation parameters in a least squares manner. Fast performance was encouraged through initializing each iterative optimization with the last known probe orientation. Machine learning regression models (e.g., deep learning, random forest) could alternatively be trained to implicitly learn the physical motion by learning the model on either real or synthetic data with known orientations [27], [28]. Although these models would require significantly more memory to store the parameter set, robust learning through large datasets may improve system performance.

Enabled by the rapid wide-area scanning, the dense spatial chromophore distributions yielded interesting observations in the *in vivo* occlusion protocol. Chromophore concentration and oxygenation values during baseline and occlusion protocols were commensurate with existing lower limb manipulation studies [29], [30]. There were marked differences in perfusion changes in the gastrocnemius medial head compared to the sur-rounding areas. Striated patterns were observed in the top calf scattering (μ_s') map. This dense map may be revealing the underlying distribution of muscle fibers that make up the large muscle group. The gastrocnemius is predominantly composed of type II fast twitch (or “white”) muscle fibers to enable fast leg movements such as running and jumping [31]. Compared to type I oxidative slow twitch fibers which require oxidative phosphorylation to generate adenosine triphosphate (ATP), type II

muscle fibers produce ATP primarily through anaerobic glycolysis, resulting in reduced perfusion and capillary networks, and thus giving it a white coloration. Furthermore, type II fibers generally have a large diameter to generate large forces and store glycogen, making it feasible to image at a macroscopic level. Monitoring muscle composition and fiber characteristics can be used to assess performance [32] and healthy aging [33], and may have implications in vascular occlusion diseases such as peripheral artery disease, thrombosis, and vascular aneurysm, in all of which blood flow and perfusion is chronically impaired. Further investigation is needed to investigate the link between these optical property patterns and muscle fiber composition.

A systemic response to left leg occlusion was observed, resulting in changes in right leg perfusion. Right leg total hemoglobin concentration did not change significantly compared to control, confirming maintained blood flow through the unobstructed leg, and yet a significant increase in deoxyhemoglobin concentration, and a resulting in oxygen saturation, was observed. Systemic effects of local vascular manipulations have been demonstrated in other cases, such as cold pressor tests causing systemic sympathetic activation and increased blood pressure [34], and leg blood flow restrictions during exercise increasing cardiac work [35]. Identifying changes in perfusion patterns in non-occluded limbs may help elucidate systemic responses to local manipulations.

In the present study, the probe position was tracked in a fixed camera coordinate system. Different camera orientations showed rotation of the probe trajectory compared to the scene coordinate system. In practice, this tilting is inconsequential, since the optical property maps generated by the probe trajectory are projected onto the scanning surface according to the camera's parameterized calibration matrix. Thus, the visual feedback to the operator is robust to camera orientations, as they may visualize the tissue properties under many different relative camera-tissue orientations as long as the target model is visible to the camera. This system may be used by operators to provide real-time tissue property feedback without the burden of adhering to a landmark-based grid system for co-aligning the data to previous patient visit scans. By addressing the primary challenges currently limiting the widespread clinical adoption of biophotonic tissue assessment, this technology can enable fast, safe, non-intrusive, and portable quantitative assessment of tissue disease assessment and monitoring, ultimately providing new technologies for preventive disease monitoring.

V. CONCLUSION

A co-integrative diffuse optical spectroscopic imaging (DOSI) system was proposed for non-gridded handheld sub-surface optical property map generation across wide areas. Tis-sue optical properties were assessed using frequency domain photon migration model, and an overhead imaging system was used to track the 3D probe measurement coordinates across time. The data were fused to generate a spatial optical property map across a region of interest. Sub-millimeter probe position estimation accuracy was demonstrated using pre-programmed probe trajectory paths, and the estimation was robust to different probe movement speeds ranging from

1.0–3.8 cm/s. The superiority of dense optical property maps using free-form non-gridded trajectories was demonstrated in a tumor inclusion tissue mimicking phantom, as well as *in vivo* in a leg cuff occlusion protocol. The optical property maps demonstrated relevant differences in scattering, absorption and chromophore concentrations in identifying the absorbing tumor inclusion and different perfusion levels with and without arterial leg occlusion. These results demonstrate an optical imaging technique that can pro-vide relevant wide area tissue information to clinical operators for enabling real-time diagnostic capabilities.

ACKNOWLEDGMENT

B. J. Tromberg reports patents, which are owned by the University of California and licensed to commercial entities that are related to the technology and analysis methods described in this study. This research was completed without their participation, knowledge, or financial support and data were acquired and processed from patients by coauthors unaffiliated with any commercial entity.

REFERENCES

[1] F. Bevilacqua et al., "Broadband absorption spectroscopy in turbid media by combined frequency-domain and steady-state methods," Appl. Opt., vol. 39, no. 34, pp. 6498–6507, 2000.

[2] G. Ganesan et al., "Diffuse optical spectroscopic imaging of subcutaneous adipose tissue metabolic changes during weight loss," Int. J. Obesity, vol. 40, no. 8, pp. 1292–1300, 2016.

[3] B. J. Tromberg et al., "Assessing the future of diffuse optical imaging technologies for breast cancer management," Med. Phys., vol. 35, no. 6 Part1, pp. 2443–2451, 2008.

[4] H. M. Peterson et al., "*In vivo* noninvasive functional measurements of bone sarcoma using diffuse optical spectroscopic imaging," J. Biomed. Opt., vol. 22, no. 12, 2017, Art. no. 121612.

[5] J.H.Lam et al., "Non-invasive dual-channel broadband diffuse optical spectroscopy of massive hemorrhage and resuscitative endovascular bal-loon occlusion of the aorta (REBOA) in swine," Military Med., vol. 183, no. suppl_1, pp. 150–156, 2018.

[6] R. V. Warren et al., "Noninvasive optical imaging of resistance training adaptations in human muscle," J. Biomed. Opt., vol. 22, no. 12, p. 1, 2017.

[7] B. J. Tromberg et al., "Predicting responses to neoadjuvant chemother-apy in breast cancer: ACRIN 6691 trial of diffuse optical spectroscopic imaging," Cancer Res., vol. 76, no. 20, pp. 5933–5944, 2016.

[8] A. E. Cerussi et al., "Frequent optical imaging during breast cancer neoad-juvant chemotherapy reveals dynamic tumor physiology in an individual patient," Academic Radiol., vol. 17, no. 8, pp. 1031–1039, 2010.

[9] A. E. Cerussi et al., “Diffuse optical spectroscopic imaging correlates with final pathological response in breast cancer neoadjuvant chemotherapy,” Philos. Trans. Roy. Soc. A, vol. 369, no. 1955, pp. 4512–4530, 2011.

[10] H. S. Yazdi et al., “Mapping breast cancer blood flow index, composi-tion, and metabolism in a human subject using combined diffuse optical spectroscopic imaging and diffuse correlation spectroscopy,” J. Biomed. Opt., vol. 22, no. 4, 2017, Art. no. 045003.

[11] R. Choe et al., “Diffuse optical tomography of breast cancer during neoadjuvant chemotherapy: A case study with comparison to MRI,” Med. Phys., vol. 32, no. 4, pp. 1128–1139, 2005.

[12] C.-Y. Wang et al., “Diffuse optical multipatch technique for tissue oxy-genation monitoring: Clinical study in intensive care unit,” IEEE Trans. Biomed. Eng., vol. 59, no. 1, pp. 87–94, Jan. 2012.

[13] D. T.-P. Fong and Y.-Y. Chan, “The use of wearable inertial motion sensors in human lower limb biomechanics studies: A systematic review,” Sensors, vol. 10, no. 12, pp. 11556–11565, 2010.

[14] W. T. Ang, P. K. Khosla, and C. N. Riviere, “Design of all-accelerometer inertial measurement unit for tremor sensing in hand-held microsurgi-cal instrument,” in Proc. IEEE Int. Conf. Robot. Autom., vol. 2, 2003, pp. 1781–1786.

[15] S.-E. Wei et al., “Convolutional pose machines,” in Proc. IEEE Conf. Comput. Vision Pattern Recognit., 2016, pp. 4724–4732.

[16] M. Danelljan et al., “Convolutional features for correlation filter based visual tracking,” in Proc. IEEE Int. Conf. Comput. Vision, 2015, pp. 58–66.

[17] T. M. Peters, “Image-guidance for surgical procedures,” Phys. Medi. Biol., vol. 51, no. 14, pp. R505–R540, 2006.

[18] E. Papi et al., “Spinal segments do not move together predictably during daily activities,” Gait Posture, vol. 67, pp. 277–283, 2018.

[19] A. E. Cerussi et al., “Tissue phantoms in multicenter clinical trials for diffuse optical technologies,” Biomed. Opt. Express, vol. 3, no. 5, pp. 966–971, 2012.

[20] R. C. Haskell et al., “Boundary conditions for the diffusion equation in radiative transfer,” J. Opt. Soc. Am. A, vol. 11, no. 10, pp. 2727–2741, 1994.

[21] Z. Zhang, “A flexible new technique for camera calibration,” IEEE Trans. Pattern Anal. Mach. Intell., vol. 22, no. 11, pp. 1330–1334, Nov. 2000.

[22] J. Heikkila and O. Silven, “A four-step camera calibration procedure with implicit image correction,” in Proc. IEEE Conf. Comput. Vision Pattern Recognit., 1997, pp. 1106–1112.

[23] A. Geiger et al., “Automatic camera and range sensor calibration using a single shot,” in Proc. IEEE Int. Conf. Robot. Autom., 2012, pp. 3936–3943.

[24] T. Yang, Finite Element Structural Analysis. Englewood Cliffs, NJ, USA: Prentice-Hall, 1986.

[25] D. Watson, Contouring: A Guide to the Analysis and Display of Spatial Data. vol. 10, Amsterdam, The Netherlands: Elsevier, 2013.

[26] N. Haghany, "A portable broadband, multi-channel instrument for frequency-domain diffuse optical spectroscopy and imaging," Ph.D. dis-sertation, Univ. California, Irvine, 2013.

[27] G. Pavlakos et al., "6-DoF object pose from semantic keypoints," in Proc. IEEE Int. Conf. Robot. Autom., 2017, pp. 2011–2018.

[28] M. Rad et al., "Feature mapping for learning fast and accurate 3D pose inference from synthetic images," in Proc. IEEE Conf. Comput. Vision Pattern Recognit., 2018, pp. 4663–4672.

[29] G. Ganesan et al., "Effect of blood flow restriction on tissue oxygenation during knee extension," Med. Sci. Sports Exer., vol. 47, no. 1, p. 185, 2015.

[30] E. Ohmae et al., "Sensitivity correction for the influence of the fat layer on muscle oxygenation and estimation of fat thickness by time-resolved spectroscopy," J. Biomed. Opt., vol. 19, no. 6, 2014, Art. no. 067005.

[31] L. Whittier, Anatomy & Physiology. Open Oregon State, Oregon State Univ., Corvallis, OR, USA, 2018.

[32] P. M. Clarkson et al., "Maximal isometric strength and fiber type composi-tion in power and endurance athletes," Eur. J. Appl. Physiol. Occupational Physiol., vol. 44, no. 1, pp. 35–42, 1980.

[33] K. S. Nair, "Aging muscle," Amer. J. Clin. Nutrition, vol. 81, no. 5, pp. 953–963, 2005.

[34] E. A. Hines Jr and G. E. Brown, "The cold pressor test for measuring the reactibility of the blood pressure: Data concerning 571 normal and hypertensive subjects," Amer. Heart J., vol. 11, no. 1, pp. 1–9, 1936.

[35] C. P. Renzi et al., "Effects of leg blood flow restriction during walking on cardiovascular function," Medicine Sci. Sports Exercise, vol. 42, no. 4, p. 726, 2010.

This work was supported in part by the Natural Sciences and Engineering Research Council of Canada under Grant PDF-503038-2017, in part by the National Institute of Biomedical Imaging and Bioengineering under Grant P41EB015890, in part by the Military Medical Photonics Program AFOSR under Grant FFA955017-1-0193, and in part by the Arnold and Mabel Beckman Foundation. (Corresponding author: Robert Amelard.)

R. Amelard is with the Schlegel-UW Research Institute for Aging, Waterloo, ON N2J 0E2, Canada (e-mail: ramelard@uwaterloo.ca).

J. H. Lam and A. Durkin are with Beckman Laser Institute and Medical Clinic, University of California, Irvine.

B. Hill and B. J. Tromberg were with Beckman Laser Institute and Medical Clinic, University of California, Irvine. They are now with the Eunice Kennedy Shriver National Institute of Child Health and Human Development, National Institutes of Health.

K. Cutler was with Beckman Laser Institute and Medical Clinic, University of California, Irvine, Irvine.

This article has supplementary downloadable material available at http://ieeexplore.ieee.org.

Digital Object Identifier 10.1109/TBME.2019.2950004